

# Facility Diagnostic Beamline Preliminary Design Report

**6.2.79.1 Rev. 1**

Date: 02-Aug-01

**Copyright 2002, Canadian Light Source Inc.** This document is the property of Canadian Light Source Inc. (CLSI). No exploitation or transfer of any information contained herein is permitted in the absence of an agreement with CLSI, and neither the document nor any such information may be released without the written consent of CLSI.

Canadian Light Source Inc.  
101 Perimeter Road  
University of Saskatchewan  
Saskatoon, Saskatchewan Canada

Signature

Date

***Original on File – Signed by:***

Author

\_\_\_\_\_  
J. C. Bergstrom

\_\_\_\_\_

Reviewer #1

\_\_\_\_\_  
I. Blomqvist

\_\_\_\_\_

Reviewer #2

\_\_\_\_\_  
T. May

\_\_\_\_\_

Approver

\_\_\_\_\_  
E. Hallin

\_\_\_\_\_

---

## REVISION HISTORY

---

<i>Revision</i>	<i>Date</i>	<i>Description</i>	<i>Author</i>
A	02-APR-1	Original Draft	J.C. Bergstrom
0	02-Jul-8	Conceptual Design Report Issued for use.	J.C. Bergstrom
1	02-Aug-01	Preliminary Design Report Issued for use.	J.C. Bergstrom

## Table of Contents

<b>1.0</b>	<b>General Overview .....</b>	<b>1</b>
	1.1 ... Introduction.....	1
	1.2 ... Source-Point Machine Functions .....	3
	1.3... Electron Beam Emittance .....	4
	1.4... Curvature Limit.....	4
	1.5... Diffraction Limit .....	5
	1.6... Depth of Field Limit .....	5
	1.7... Vertical Opening Angle of the Synchrotron Radiation .....	6
	1.8... Instrumentation Priorities .....	7
<b>2.0</b>	<b>The OSR Beamline .....</b>	<b>8</b>
	2.1 ... Power Density and Fixed Aperture .....	8
	2.2... Emittance Measurement .....	9
	2.3... Primary Mirror .....	9
	2.4... Primary Mirror Thermal Distortion .....	10
	2.5... Transmission to the Optical Table .....	12
	2.6... Vacuum-to-Air Transition .....	12
	2.7... Secondary Mirror.....	12
	2.8... Focusing System.....	13
	2.9... Primary Slits .....	14
	2.10 . Filters and Intensity Control.....	15
	2.11 . Optical Table .....	16
	2.12 . OSR Instrumentation: Phase I.....	17
	2.12.1 Intensified Gated Charge-Coupled Detector Camera. ....	18
	2.12.2 Ungated Charge-Coupled Camera .....	19
	2.12.3 MCP-Intensified Photomultiplier Tube; Avalanche Photodiode Detector ...	19
	2.12.4 Position Detector.....	20
	2.12.5 Fast Photodiode; Sampling Optical Oscilloscope .....	20
	2.13 . OSR Instrumentation: Phase II.....	21
	2.14 . Optical Pulse-Length With a Finite Aperture.....	23
	2.15 . Focusing and Calibration .....	23
<b>3.0</b>	<b>The XSR BEAMLINE.....</b>	<b>25</b>
	3.1 ... Introduction.....	25
	3.2... Front End and the Power Density .....	26
	3.3... Exit Window .....	26
	3.4... Pinhole slits .....	27
	3.5... Transfer line.....	28
	3.6... Imaging System .....	29
	3.7 ... Emittance Measurement .....	31
	3.7.1 Vertical Electron Emittance.....	32
	3.7.2 Horizontal Electron Emittance.....	33
	3.8... Limits to Resolution .....	34
	3.8.1 Diffraction Limitations .....	34
	3.8.2 Emittance and Coupling Resolution.....	36
<b>4.0</b>	<b>Report Summary.....</b>	<b>37</b>



## 1.0 GENERAL OVERVIEW

### 1.1 INTRODUCTION

The functions of the Facility Diagnostic Beamline (FDB) are to determine various stable-beam qualities, to determine unstable-beam characteristics, and to facilitate studies of the transverse and longitudinal beam dynamics. Below, we summarize some of the desired measuring capabilities of the FDB.

1. Photon beam size in both planes, and the photon angular spread. These quantities define the photon beam emittance, and hence the intrinsic brightness of the source point.
2. Use the photon measurements (visible and x-ray) to deduce the electron beam size, phase-space ellipse and emittance. Deduce the first and second moments of the beam distribution in the transverse plane.
3. Photon source-point positional stability. This provides a measure of transverse beam instabilities.
4. Determine the x-y emittance coupling. Indications from the User community suggest that 1% coupling is (currently) the acceptable upper limit.
5. Determine the longitudinal emittance of the electron beam (energy spread and bunch length). Deduce the first and second moments of the beam distribution in the longitudinal direction.
6. In a single-bunch mode, machine studies include:
  - i. RF bunch purity
  - ii. Bunch length vs. current
  - iii. Energy spread vs. current
  - iv. Bunch length vs. RF voltage
  - v. Transverse beam size vs. current, which provides a measure of the ring impedance.
  - vi. Diagnostics of head-tail instabilities
7. In a multi-bunch mode, machine studies include some of the items under (6), plus the following:
  - i. Diagnostics of coupled-bunch instabilities
  - ii. Diagnostics of longitudinal instabilities using a dispersive source-point
  - iii. Bunch-phase stability re the cavity RF.

8. Measure transient beam motion following injection, before the beam has damped. This will assist in optimizing the injection system, which is especially crucial for a top-up mode of operation. Note that the FDB must operate *during* injection (unlike the other beamlines).
9. Measure the transverse bunch extent on a turn-by-turn basis immediately following injection. This will assist in matching the Twiss parameters of the injected beam to those of the ring ("beam matching"). Studies suggest that matching the vertical ( $y$ )  $\beta$ -function is especially important for maximizing the capture efficiency. These remarks also apply to the Booster.
10. Measure the circulating beam energy by employing the method of Resonant Depolarization. This well-known technique yields the absolute energy (mean), with relative accuracies of  $10^{-4}$  to  $10^{-5}$  being achievable.

Our concepts for the FDB have been guided by a study of similar beamlines at other facilities (APS, ALS, NSLS, ESRF, Max II, and others). Details have been gleaned from the proceedings of various international symposia, such as PAC, BIW, and EPAC. Discussions with Bingxin Yang at the APS have been especially helpful.

Our first conclusion is that in order to comply with the above requirements, the FDB will need both visible synchrotron radiation (OSR) and x-ray (XSR) capabilities. We have further concluded that the source point should be provided by dipole magnets, and not by an undulator. Finally, the OSR and XSR source points will be located within two different dipole magnets. These magnets are the two dipoles of Cell-2. The OSR source point is  $5^\circ$  in from the entrance of the first dipole (B1), while the XSR source point is  $4^\circ$  in from the entrance of the second dipole (B2). The straight section preceding the two dipoles, often called the "diagnostic straight," will be occupied by machine diagnostic apparatus (BPMs, tune kickers, etc.).

We had been advised by the APS to keep the OSR line as short as possible. Among other things, this would permit imaging by lenses rather than mirrors (lenses suffer from chromatic aberrations which become a limiting factor for long optical lines). Thus, placing the OSR diagnostics on the Storage Ring tunnel roof became an attractive option, but inspection of the available real estate, constrained as it is by a miscellany of pipes and cable trays quickly ruled out this option.

Therefore, both the OSR and XSR end-stations will necessarily occupy space exterior to their respective forward-walls. This immediately brings up the question of whether or not end-station enclosures are required. Human safety factors are not an issue in dictating the enclosure for the OSR line since no x-rays are brought to the optical table, and hence such an enclosure would not be lead-lined. The situation on the XSR line is still undefined. On the other hand, equipment

safety might indeed be an issue. Walkways past the end-stations are an obvious threat to equipment integrity. Temperature stability of the end-station apparatus may require an enclosure if the ambient standard of  $\pm 1^\circ\text{C}$  is not met. Conclusion: The OSR end-station should be enclosed within a light-tight, temperature stabilized, acoustically insulated and dust-free environment, at least to the degree dictated by practical considerations. Standard services, such as electrical power and compressed air will be required (but not cryogenic delivery).

Next, we review the various electron and photon parameters that constrain the design of the FDB optical beamlines and the end-station instrumentation. These parameters are essentially defined by the basic lattice design and hence are not flexible.

## 1.2 SOURCE-POINT MACHINE FUNCTIONS

The machine functions (Twiss parameters) at the OSR and XSR source points are listed here in the usual units (meters, etc.) (priv. com. Les Dallon, as of April 20, 2002). We refer here to the electron beam, not the photon beam. As noted above, the OSR and XSR source points are, respectively,  $5^\circ$  in from the entrance of dipole-1 and  $4^\circ$  in from the entrance of dipole-2, of Cell-2. For future reference, the bending radius of the dipole magnets is  $\rho = 7.143$  m.

OSR source point:

$$\begin{aligned} \beta_x &= 1.10 & \alpha_x &= 0.96 \\ \beta_y &= 25.08 & \alpha_y &= -4.57 \\ \eta_x &= 0.064 & \eta_x' &= 0.021 \end{aligned} \tag{1}$$

XSR source point:

$$\begin{aligned} \beta_x &= 0.75 & \alpha_x &= 0.46 \\ \beta_y &= 26.29 & \alpha_y &= -3.07 \\ \eta_x &= 0.127 & \eta_x' &= -0.150 \end{aligned} \tag{2}$$

One notes the large differential between  $\beta_x$  and  $\beta_y$  at the source points. The large values of  $\beta_y$ , actually close to the maximum values anywhere in the lattice, are crucial to obtaining the highest possible measurement resolution of the beam size in the vertical plane. The large  $\beta_y$  derive from the quadrupole (gradient) components in the dipole magnets, in contrast to the  $\beta$ -function observed in a uniform dipole magnet.

### 1.3 ELECTRON BEAM EMITTANCE

The horizontal emittance  $\epsilon_x$  is a strong function of how the lattice is tuned. For example, if the dispersion function is tuned to  $\eta_x = 0$  in the straight sections, then  $\epsilon_x = 31$  nm-rad, but by tuning for  $\eta_x = 0.15$ m the horizontal emittance is reduced to the (operational) value

$$\epsilon_x = 18.2 \text{ nm-rad.} \quad (3)$$

Our discussion will assume the x-y- emittance coupling is 1%, so

$$\epsilon_y = 0.18 \text{ nm-rad.} \quad (4)$$

We will adopt Eq.(3) and Eq.(4) in the following analysis.

The intrinsic size of the electron beam at the OSR and XSR source points can now be estimated using Eqs.(1-4). Both source points have finite dispersion ( $\eta_x$ ), so the natural energy spread of the beam ( $\pm\delta$ ) will further contribute to the source width. The damped energy spread is  $\delta = \pm 0.1\%$ . The intrinsic beam sizes (diameters) are estimated as follows, where we define the size of the distributions by the standard deviation of the gaussian distributions:

OSR source point

$$2\sigma_x = 308 \text{ (282) } \mu\text{m} \quad (5)$$

$$2\sigma_y = 134 \mu\text{m (1\% coupling).}$$

XSR source point

$$2\sigma_x = 344 \text{ (232) } \mu\text{m} \quad (6)$$

$$2\sigma_y = 136 \mu\text{m (1\% coupling).}$$

The quantities in brackets are the source diameters in the limit  $\delta = 0$ .

### 1.4 CURVATURE LIMIT

The above intrinsic electron beam profiles are further augmented by the horizontal broadening due to the curvature of the electron orbit within the lattice dipoles. The apparent broadening of the photon source is a function of the *total* horizontal angular acceptance  $\theta$  of the beamline. The contribution to the photon source width is given by

$$W_c = \rho\theta^2 / 8. \quad (7)$$

The dipole vacuum chamber lets through a fan width of about  $\theta = 10$  mrad, so Eq.(7) gives the curvature limit for the OSR line

$$W_c = 89 \mu\text{m.} \quad (8)$$

Actually, this limit will be much reduced by the constraints imposed by the more severe Depth of Field Limit (below), which requires the fan width to be reduced to about  $\theta = 4$  mrad total.

## 1.5 DIFFRACTION LIMIT

Synchrotron light is concentrated in a narrow forward cone, and is thus subject to diffraction phenomena similar to that of an isotropic source collimated by a narrow aperture. This diffraction limits the ultimate resolution of any scheme devised to measure the size of the photon source. Various estimates exist for the diffraction-limited spatial resolution (see for example Yang and Lumpkin, B.I.W. 1994, p.252; Fisher, B.I.W. 1998, p.95). We employ the estimate given by Fisher:

$$W_d = 2 \times 0.26 (\rho \lambda^2)^{1/3}. \quad (9)$$

where  $\rho$  is the bending radius and  $\lambda$  is the wavelength of the light (both in the same units). Note that  $W_d$  is the diffraction spot size (diameter), to be compared with the photon source sizes of Eq.(5) and Eq.(6). This particular diffraction limitation is not an issue for the XSR beamline ( $\lambda \approx 0.1$  nm), but is not negligible in the optical (OSR) region. The diffraction limit (spot diameter) over the region  $\lambda = 200 - 600$  nm, is

$$\begin{aligned} W_d &= 34 \text{ } \mu\text{m} & \lambda &= 200 \text{ nm} \quad (6.2 \text{ eV}) \\ W_d &= 72 \text{ } \mu\text{m} & \lambda &= 600 \text{ nm} \quad (2.1 \text{ eV}) \end{aligned} \quad (10)$$

These values also define the ultimate source resolution when the system magnification is unity.

## 1.6 DEPTH OF FIELD LIMIT

As previously noted, the curvature of the electron orbit within the dipole magnets contributes to the apparent *width* of the beam, due to the finite total horizontal acceptance  $\theta$  of the beamline. The curvature and acceptance also contribute to the apparent *length*  $L$  of the source:

$$L = \rho \theta,$$

where the natural opening angle of the photon beam (which of course also contributes to  $L$ ) is ignored here. (We will argue this point later).

Confining the discussion to OSR, consider an imaging system consisting of a single lens (for simplicity) situated a distance  $d_1$  from the source point, while the image is formed at a distance  $d_2$  from the lens. A point source ( $L = 0$ ) would produce a point image, but adjacent point sources distributed along a finite  $L$  would produce images that are out of focus at  $d_2$ . Since the apparent source length is  $L$  for both horizontal and vertical imaging, the out-of-focus image would appear as a disk of diameter

$$W_{df} = (\rho\theta^2 / 2) (d_2 / d_1). \quad (11)$$

Note that for  $d_2 \approx d_1$ , the above is *four times* the curvature limit, Eq.(7). Since the optical magnification is given by  $M = d_2 / d_1$ , one does not gain by minimizing the ratio  $d_2 / d_1$  in Eq.(11).

For  $\rho = 7.15$  m,  $\theta = 10$  mrad, and  $d_2 = d_1$ , we get

$$W_{df} = 358 \text{ } \mu\text{m}. \quad (12)$$

This is by far the largest contribution to the imaging resolution in both planes. *Aperture restriction in the horizontal plane will clearly be necessary to reduce  $q$ , and hence  $W_{df}$ .* In fact, we will opt for a total horizontal acceptance of  $\theta = 4\text{-}6$  mrad (see Sect. 2.9 below). For comparison, the horizontal acceptance of the OSR lines at other facilities (by our reading of the literature) is as follows: APS (3.5 mrad, 6 mrad), ALS (1 mrad, 2 mrad), ESRF (10 mrad).

Actually, the depth of field limitation defined by Eq. (11) is somewhat pessimistic since it ignores the actual intensity distribution across the disk of diameter  $W_{df}$ . A simple argument demonstrates that the distribution should be more of a Gaussian shape than uniform. Thus, the final image could be considered as the superposition of a large number of disks of varying radii, each containing the same number of photons and each originating from a different source point distributed along  $L$ . For a Gaussian-like intensity distribution, the depth of field limit will certainly be less than implied by Eq. (11) and Eq. (12).

The natural opening angle of the synchrotron radiation can also contribute to  $L$ , and therefore to the depth of field limit. If this angle is large compared to the angular acceptance of the slit system, the “search-light” beam of radiation will sweep across the slits with increasing, then decreasing intensity. The result is a Gaussian-like transmitted intensity distribution as *a function of the source position along  $L$* . However, consideration of the energetics associated with the OSR beamline shows that the photon-opening angle is actually much smaller than the slit acceptance. The sweep function therefore more closely resembles a step function, and the opening angle can be ignored, as suggested above.

## 1.7 VERTICAL OPENING ANGLE OF THE SYNCHROTRON RADIATION

The nominal wavelengths of the synchrotron radiation in the OSR and XSR beamlines are:

$$\text{OSR: } \lambda = 600 \text{ nm}$$

$$\text{XSR: } \lambda = 0.10 \text{ nm.}$$

The latter corresponds to 12 keV radiation, although the brightness spectrum actually peaks slightly lower, at about 6 keV.

The vertical profile has been calculated as a function of the vertical angle  $\psi$  for both the horizontal ( $\sigma$ ) and vertical ( $\pi$ ) polarization components using the code SHADOW (courtesy of Brian Yates).

The  $\pi$  component (which resembles two side-by-side Gaussians and vanishes at  $\psi = 0$ ) is much weaker than the  $\sigma$  component, especially in the x-ray region. The observations below apply to the sum of the two components, which is definitely Gaussian-shaped for the XSR, but less so for the OSR.

The vertical angular aperture in  $\psi$  is given here as a function of the angular cut-off, expressed as a multiple of the Gaussian width parameter  $\sigma$ .

OSR

$\pm 1 \sigma$	$\pm 2.17$ mrad	
$\pm 2 \sigma$	$\pm 3.49$ mrad	(13a)
$\pm 3 \sigma$	$\pm 4.56$ mrad	

XSR

$\pm 1 \sigma$	$\pm 0.084$ mrad	
$\pm 2 \sigma$	$\pm 0.155$ mrad	(13b)
$\pm 3 \sigma$	$\pm 0.216$ mrad	

For reference, we note that the percentage of the total area contained within  $\pm 1 \sigma$ ,  $\pm 2 \sigma$ , and  $\pm 3 \sigma$  are 68.3%, 95.4% and 99.7%, respectively. Actually, these percentages have been used to *define* the effective  $1\sigma$ ,  $2\sigma$ ,  $3\sigma$  widths, from the *actual* vertical angular distribution function. Thus, the above numbers reflect a breakdown of the strictly Gaussian approximation for the vertical angular distribution.

The vertical angular aperture as defined by the B1dipole vacuum chamber is  $\psi = \pm 4.33$  mrad, which is slightly smaller than the  $3\sigma$  limit for the OSR.

## 1.8 INSTRUMENTATION PRIORITIES

The *eventual* desired measuring capabilities of the FDB were described in Section 1.1. The follow-up issue addresses which instrumentation should have the highest developmental priority in the early stages. Here we will present generalities: later a more specific device description will be given. During storage ring commissioning, for example, the beam will be low (a few mA) and will be moving around a lot. First priority should therefore be given to a camera operating in the OSR region, with a reasonable field of view, and preferably fast-gated to permit turn-by-turn information. This compliments the BPM system but has greater sensitivity at very low currents.

In addition, an ordinary ungated CCD camera would be a useful complement to monitor the beam behavior averaged over many turns.

Next in overall priority is an x-ray pinhole camera, with a high dispersion source point. This device has a much higher spatial resolution than the above OSR system, but also has a much smaller field of view, which makes it useful only after the orbit of the electron beam has been stabilized. With a high dispersion source point we gain information on both the transverse and longitudinal aspects of the beam. (From Eq. (2), the dispersion at the source point is 0.127 m.)

The XSR pinhole beamline is rather simple in conception. Following the appropriate front-end hardware is the pinhole aperture. Further down the beamline is the converter crystal (YAG: Ce), which converts the x-ray pinhole image to the visible region. This is immediately followed by a CCD camera to record the image.

The final major piece of diagnostic instrumentation is the so-called “streak camera”, also to be located on the OSR beamline. Although it does not have a spatial resolution capability as good as the fast-gated camera at the top of our list, the time resolution is unsurpassed at 2 ps. The dual-sweep streak camera is the only real option for measuring the bunch length of the damped beam, about 54 ps ( $2\sigma$ ). The ability to ‘photograph’ single bunches from the front, top or side, and thus visually observe the onset of various beam instabilities, makes this an extremely useful analytical tool. However, unlike the gated camera and the pinhole camera, the streak camera is of little interest to the “user community” and falls solely within the domain of accelerator physics analysis. We expect the streak camera will be most useful during the more-or-less routine operation of the storage ring, and is not an essential component of the early commissioning phase of the storage ring. The essential devices (described later) we will classify as Phase I instrumentation. Follow up instrumentation, such as the streak camera, falls within a later Phase II. The XSR pinhole beamline will also fall within Phase II.

## 2.0 THE OSR BEAMLINE

### 2.1 POWER DENSITY AND FIXED APERTURE

At 500 ma, the total radiation power from the dipole source-point translates into 70 Watts per horizontal mrad, integrated over the vertical angle. This power is concentrated in the high-frequency domain, near the critical energy (roughly 7 keV). The x-ray fan is therefore a significant factor in the heat-load on the subsequent optical elements. *We propose to delimit the horizontal angular extent of the radiation to 4-6 mrad (total width) by a fixed aperture in the dipole magnet vacuum chamber, but will not alter the vertical acceptance as defined by the chamber, namely 8.6 mr total. The heat-load on the first optical element is thus 280-420 Watts, assuming*

*total absorption of the radiation, which is clearly excessive.* The horizontal acceptance reduces considerably the Depth of Field Limit described in Section 1.6 (Eq. 11-12). Other options are discussed in Sect. 2.9 below.

## 2.2 EMITTANCE MEASUREMENT

The resolution of the OSR Line is not sufficient to provide anything but a very marginal measure of the horizontal and vertical beam emittances, except perhaps during early machine commissioning when large emittance excursions might be expected. To quantify the expected resolution, we will assume a horizontal angular acceptance of 4 mrad. Then combining the curvature limit, diffraction limit and depth-of-field limit in quadrature yields a resolution diameter of about 90  $\mu\text{m}$ . This is totally dominated by the depth-of-field limit and the diffraction limit. Using Eq. (5), the  $\beta$  functions of Eq. (1), and the usual relation between beam size and emittance, the resolution on emittance measurement is estimated to be about 13 nm in the horizontal plane, and 0.23 nm in the vertical plane, commensurate with the actual design emittances of Eq. (3) and Eq. (4). The situation improves if the horizontal acceptance is reduced to the point where the diffraction limit [Eq. (10)] dominates over the other limits, but one only gains by about a factor of two in the emittance resolution. More precise emittance measurements will require the x-ray line (XSR).

## 2.3 PRIMARY MIRROR

The OSR line has no “front-end” in the usual sense, since only visible radiation is to be transmitted to the “end station”. The dipole magnet radiation is thus transmitted directly to the first optical element of the OSR. The technical issue is how to deal with the hot x-ray fan, which by far dominates the power spectrum. Thus, of the total of 70 Watts/mrad of radiation power mentioned above, the OSR component is only about 1.4 milliWatts/mrad ( $\lambda = 400 - 900 \text{ nm}$ ). A power load of 280 Watts is sufficient to distort the primary mirror well beyond our flatness tolerance.

Various options for dealing with the x-ray fan were addressed in the Conceptual Design Report 6.2.79.1. The scheme that will be implemented is now described. A schematic layout of the optical chicane is shown in Fig. 1.

Synchrotron radiation travels 5 m from the dipole source point to a planar (primary) mirror, which directs the visible light  $90^\circ$  downward 0.5 m to the secondary mirror. The secondary mirror reflects the visible light  $90^\circ$ , placing it on a forward horizontal path through the focusing lens and onward to the optical table.

The primary mirror is situated such that it intercepts only the top half of the radiation fan, and is pulled upward sufficiently to allow the hot x-ray core to pass beneath. The lower edge is necessarily bevelled at a 45° angle, and will support a thermo-probe, which will sense the proximity of the x-ray core. A closed-loop feedback system will control the mirror position using a motorized translation stage whose travel is parallel to the surface of the mirror. This scheme offers better protection from thermal distortion due to a missteered beam than the (static) shadow finger approach. The price to be paid is that only about half the available light is directed to the optical table.

The mirror itself might consist of an aluminum coating over a nickel-plated Glidcop substrate. The aluminum mirror has been studied in detail in comparison with other materials, and is clearly superior for the purpose. For example, the reflectivity of an aluminum mirror for a 90° deflection is completely negligible for photons above 50 eV, which reduces the heat load on the secondary mirror to a negligible value.

The mirror can be relatively small: a 50 x 50 mm mirror is more than adequate to subtend the horizontal angular acceptance (4 mrad) and the now-reduced vertical acceptance (4.3 mrad). Surface flatness is usually described in terms of the wave-front distortion (the so-called Optical Path Difference) in units of the wavelength  $\lambda$  of a convenient source, such as a He-Ne laser ( $\lambda = 633$  nm). The peak-to-valley flatness of a good mirror is  $\lambda/4$ , that of superior mirror is  $\lambda/10$ , and for an excellent mirror is  $\lambda/30$ . Keeping in mind that the OPD accumulates with each succeeding optical device, a flatness of  $\lambda/10$  is a minimal requirement. The surface roughness should not exceed 1 nm (rms).

## 2.4 PRIMARY MIRROR THERMAL DISTORTION

Thermal distortion of the primary mirror for a given absorbed heat load is best evaluated using the technique of finite-element analysis. Nevertheless, useful order-of-magnitude estimates of the image distortion can be obtained from simple analytic equations (see, for example, N.I.M. A291 (1990), p. 286-299). Three general mirror distortions are evident: a general bowing of the mirror caused by the front-to-back thermal gradient, *assuming back-cooling of the substrate*; a thermal “bump” on the surface; and a shift in the spacing of the crystal planes in a diffracting crystal. The first distortion is dominant and will be the focus here (note that this particular distortion can be reduced by cooling options other than back-plane cooling).

The radius of curvature R of the thermally deformed mirror is given by

$$R(\text{m}) = \frac{k}{\alpha Q (\text{W} / \text{m}^2)}$$

where, for Glidcop, the coefficient of thermal expansion is

$$a = 16.6 \times 10^{-6} / \text{degC}$$

and the thermal conductivity is

$$k = 365 \text{ W / m-deg C.}$$

(The above values are taken from Daly et al., PAC'97, p.2014.)

Expressing the absorbed heat load in  $\text{W/mm}^2$ , we find

$$R(\text{m}) = \frac{22}{Q(\text{W/mm}^2)}.$$

The focal length of a spherical mirror of radius  $R$  is given by  $f = R/2$ . Now, the OSR focusing system consists of a single lens situated at the midpoint between the source and image positions (see below), corresponding to point-to-point optics. The thermally distorted mirror in effect introduces a second lens of focal length  $f$  between the source point and the main lens. A point source will no longer be imaged to a point, but will instead produce a blurred image of diameter  $S$ . Clearly,  $S$  is a function of  $f$  (i.e.  $R$ ), and hence is a function of the heat load  $Q$  ( $\text{W/mm}^2$ ). The relationship is given by elementary optics, and the following are deduced. Given that the source-to-mirror distance is 5 m, the mirror-to-lens distance is 1 m, and the lens-to-image distance is 6 m, one finds for a 4 mrad wide light fan

$$S(\text{mm}) = 9.1Q(\text{W/mm}^2).$$

Thus, if the image blurring is to be kept to 20% or less of the perfect image, then  $S \leq 0.025$  mm or

$$Q \leq 2.8 \text{ milliWatts/mm}^2.$$

To gain some perspective, one recalls that the total radiation power is 70 Watts/mrad, that the power in the 100 – 400 eV range is 1.1 Watts/mrad, and that the power in the “visible” region (400 – 900 nm) is about 1.4 milliWatts/mrad. Note that  $Q$  is absorbed, not reflected, power, and from previous remarks it is clear that only the x-ray component is a threat. The power density in the hot x-ray core is roughly  $9 \text{ Watts/mm}^2$ , so a careful positioning of the primary mirror is mandatory.

Water-cooling of the primary mirror is required, even if confined to a single cooling channel. This will not dissipate the heat from a steady x-ray load, but rather is intended to thermally stabilize the mirror quickly in the event of the transient x-ray “flashes” from an unstable beam.

## 2.5 TRANSMISSION TO THE OPTICAL TABLE

The reference level of the initial beam is 1.4 m above the floor. The beam is deflected 90° downward by the primary mirror through a distance of 0.5 m, where another mirror (secondary) then redirects the beam back again onto the horizontal plane, in a direction parallel to the initial beam. The beam, now 0.9 m above the floor, passes through the main focusing lens, then through a hole in the forward concrete wall, to end up at the optical table. Transmission of the OSR beam to the optical table will be at atmospheric pressure, through enclosed conduits that will remove the disturbing influence of air currents. The conduit will be terminated by a thin exit window of quartz or other appropriate OSR-transmitting material.

The vertical offset of 0.5 m is chosen as a convenient way of disposing of the x-rays, and as a way to exit the storage ring vault well off the plane of the storage ring, which is the plane of a maximum ambient radiation. We choose to deflect downward, rather than upward, to keep the optical table at low level. Besides easier access (the alternative scheme would place the table 1.9 m above the floor), the shorter table legs should reduce the vibration problems for the table, and also for the secondary mirror. Finally, there is a safety issue. The optical table must be accessible during live-beam operation. Upward deflection would place the optics close to eye level, which is potentially dangerous when making adjustments with a live beam.

## 2.6 VACUUM-TO-AIR TRANSITION

The primary mirror will be situated in vacuum contiguous with the UHV of the storage ring. On the other hand, the secondary mirror, positioned 0.5 m below, will be situated in a chamber at atmospheric pressure (STP). The juncture is provided by a sapphire window located roughly 200 – 250 mm below the primary mirror. Preliminary design suggests a circular window 50 mm in diameter and 1 mm thick. Hydrostatic burst pressure of this window by the manufacturer is quoted as 24 psi, but this value also incorporates a safety factor of three. The properties that recommend sapphire are its extreme hardness, its high thermal conductivity, and its fundamental optical characteristics.

Since the window is situated near the primary mirror, the flatness requirement should be comparable to that of the mirror (i.e. about  $\lambda/10$ ). Note that both surfaces of the window must be taken into account.

## 2.7 SECONDARY MIRROR

The secondary mirror is situated 0.5 m below the primary mirror, in a chamber at atmospheric pressure. It can be a copy of the primary mirror (50 x 50 mm; aluminum over a nickel-coated Glidcop substrate, although this may be “overkill” in view of the low power density on this mirror).

This mirror controls alignment of the light beam onto the optical table, about 6 – 7 m downstream, and therefore *must be mounted on a high-resolution tilt-rotate platform*. The platform will be controlled by D.C. or stepping motors, since this mirror is inside the storage ring tunnel. Three degrees of motion are required: mirror tilt, rotation about the vertical axis, and up-down motion (a few centimeters). Commercial devices can provide tilt-rotation resolutions at a level of 10  $\mu\text{rad}$ , which translates to a resolution of 50 – 60 microns at the optical table. At present, we see no need to provide special cooling requirements for this mirror. Optical quality must be consistent with the primary mirror, namely flatness to at least  $\lambda/10$  and roughness below 1 nm (rms).

## 2.8 FOCUSING SYSTEM

Focusing of the visible light, from the dipole-magnet source point to the image plane on the optical table, will be accomplished by a simple lens system that provides a 1:1 image (unit magnification). Now, in the small-angle paraxial approximation (i.e. first order), there are no optical aberrations in a spherical lens for monochromatic light. At the next level of approximation (third order), there are five so-called Seidel aberrations for a spherical lens: spherical aberration, astigmatism, field curvature, coma, and barrel/pin cushion distortion. For a symmetric system (unit magnification), the latter two aberrations (coma and distortion) vanish, spherical aberration is minimized, and certain chromatic aberrations are significantly reduced.

One can envision several options for a symmetric 1:1 focusing system, of increasing complexity:

- A single symmetric biconvex lens, although spherical and chromatic aberrations might be problematical for small f-stops.
- Back-to-back identical plano-convex lenses, facing each other on the convex surfaces, which provides better corrections for spherical aberrations than the above single-lens option.
- Back-to-back identical cemented (two lens) achromats, which generates minimal spherical and chromatic aberrations.

We would clearly prefer that the optics be diffraction-limited rather than aberration-limited. If we adopt the single-lens option, then a large diameter lens is required. The dipole magnet source-point produces an optical fan at the lens with a radius of roughly 13 mm, assuming the lens is located at the mid point between source and image. We estimate a lens diameter of 100-150 mm is adequate. The source-to-lens distance is 6 m, so the lens focal length should be 3 m. We have not found any off-the-shelf suppliers with these parameters, although Melles Griot supplies a cemented achromatic doublet with these parameters (150 mm diameter). The problem is that this particular doublet is optimized for a conjugate ratio of infinity, not 1:1 as we require, so aberrations might be a problem if employed in the 1:1 geometry.

However, in response to our inquiries, Melles Griot provided us with a ZEMAX spot image for the above achromat in a 1:1 configuration, for  $\lambda = 550$  nm light from a Gaussian source. Since the  $f$ -stop is roughly 115 for a 3 meter focal length, the company representative suggested that we would indeed be diffraction limited, and the ZEMAX image seems to confirm this. Thus, this much cheaper off-the-shelf achromatic lens doublet may serve our purpose.

The primary focusing system must be fully adjustable by a remote stepping-motor system in 3 degrees of freedom (i.e. xyz). Longitudinal adjustment is especially important for final focusing of the system. Position adjustment of the focusing system in the longitudinal direction is defined by the depth-of-focus at the image plane. Simple geometry shows that the (aberration-free) image from a point source would increase in diameter by roughly 40 microns for a 10 mm displacement from the focal point. To shift the focus by  $\pm 10$  mm requires a shift in the lens position by about  $\pm 180$  mm, so this sets the scale for the required movement. Resolution of the longitudinal motion could be in the millimeter range, but the transverse resolution must be much better, perhaps 0.1 mm or less.

Still to be addressed is the question of how to adjust the lens in order to optimize the focus at the nominal focal position. We will return to this issue in Sect. 2.15, following discussion of the optical table layout.

## 2.9 PRIMARY SLITS

As noted elsewhere, we propose to delimit the horizontal angular extent of the radiation to about 4 mrad by means of fixed photon absorbers within the dipole magnet vacuum chamber, but allow the full vertical acceptance angle of 8.6 mrad as defined by the chamber geometry. The horizontal acceptance is constrained by the depth of field limit (see Sect. 1.6). Note also that with our proposed scheme for the primary mirror, the vertical acceptance of the *subsequent* system is cut in half, to 4.3 mr or less, *so the ultimate acceptance is roughly 4 x 4 mrad*. We may revisit the horizontal limit, perhaps increasing it to 6 mrad or so, to gather more light during storage ring commissioning, but in any case aperture considerations demonstrate the requirement for an adjustable slit system to control the angular acceptance. *We propose an independent x-y aperture control, situated close to the main focusing lens* (so that it acts as an aperture stop in the conventional sense, and thus does not distort the image). This adjustable aperture, located in air, will not be subject to the hot x-ray fan, nor (we believe) to an intense ultra-violet fan, so special cooling requirements should not be necessary. It need not be movable longitudinally, as required of the main lens. However, the issue of transverse motion of the total assembly, or independent motion of each of the four slit jaws, is still an open question.

The slits permit us to reduce the horizontal acceptance to a 1 mrad or so, which certainly improves the optics, but then we may encounter a photon statistics problem. The photon flux for a 1 mrad acceptance is discussed in Sect. 2.12 below.

## 2.10 FILTERS AND INTENSITY CONTROL

From our study of OSR lines at the other facilities, it appears to be common practice to introduce optical band-pass filters into the system (near the detectors on the optical table, to minimize image distortion), of band widths  $\Delta\lambda = 10\text{-}30$  nm, to keep the chromatic aberrations of the imaging system to a minimum. Maximum transmission is typically at  $\lambda = 550$  nm, which is also one of the favorite wavelengths of lens designers. Of course, this will considerably reduce the available light, which might be a factor during the low-current initial commissioning of the storage ring. Interchangeable filters with a wide variety of bandwidths are an option; say with bandwidths of 1% and 5% as an example.

Light intensity can be controlled by insertion of neutral-density filters of various optical densities. A simple system might consist of a set of filters that provide 0.1%, 1%, 10%, and 100% optical transmission, arranged side-by-side on a linear-drive frame. There are two kinds of neutral-density filters: absorptive filters and reflective filters. The former is preferred, providing the heat load does not lead to wave front distortion. As noted elsewhere in this report, the total power in the  $\lambda = 400\text{-}900$  nm range is about 1.4 milliWatts/mrad. Assuming  $\theta = 4$  mrad and a beam spot diameter of 200 microns on the filter, total absorption implies a heat load of roughly  $0.2 \text{ Watts/mm}^2$ . We are assuming that the filters are located on the optical table, near the detectors, in order to minimize the effects of wave-front distortions due to flatness, etc., imperfections. The heat load is well below the problematical threshold of roughly  $1 \text{ Watt/mm}^2$ .

It is advised that total attenuation be accomplished by individual filters, rather than inserting two or more units to generate the required attenuation. The reason is that multiple filters generate unwanted multiple reflections that can lead to false images.

Another option for intensity control, used for example at the Brazilian synchrotron facility (LNLS), consists of crossed dichroic polarizing screens. The advantage here is continuous control over intensity, and indeed provides total extinction of the light to the level of  $10^{-4}$ . Note that aside from the primary slits, we have so far introduced no mechanism for quenching the light on the optical table. A disadvantage of the crossed polarizer system is the *maximum* degree of light transmission. Our reading of the commercial literature suggests this is of the order of 20-35%, which may not be negligible considering that we have already discarded 50% of the available light with the primary mirror.

A singular *advantage* of the crossed polarizer scheme is that it removes, *ab initio*, the  $\pi$ -polarized component of the synchrotron light, which appears when one moves off-plane from the true horizontal midplane. As a rule one likes to remove the  $\pi$  component since it is a double-peaked distribution with a minimum in the true forward direction. In other words, even without the crossed-polarizer scheme, the  $\pi$  component should be removed by a polarizing screen. On the other hand, others (MAXLAB) have actually utilized the  $\pi$  component to achieve good resolution by clever means, but these schemes are not the off-the-shelf variety that we would adopt for the early commissioning of the CLS.

The above options for intensity control are still under review. Note that we have not mentioned utilization of the primary slit system for this purpose. While the primary slits are capable of reducing the intensity, they also cut the angular acceptance, thus modifying the curvature limit and the depth of field limit, which in turn modifies the image. Intensity control without image modification is preferred.

## 2.11 OPTICAL TABLE

The OSR instrumentation, discussed below, will be distributed across a 4 ft X 8 ft optical table located on the concrete slab immediately forward of the front face of the ratchet-like storage ring enclosure. As noted elsewhere, the beam will be transported within an enclosed conduit about 0.9 m above the floor level. The surface of the table is thus quite low, about 0.7 m above floor level.

The table thickness will be 200 mm, which is adequate to suppress most normal modes of vibration. Mounting holes will be arranged in the usual fashion with 25 mm between centers. All instrumentation will be mounted “square to the table” to simplify optical alignment. Nevertheless, appreciating that perfect alignment of the table is impossible, the posts supporting beam-splitters, mirrors, etc., will be anchored on universal bases, which permit rotational/translational motion relative to the mounting holes.

The optical centerline is 200 mm above the surface of the optical table. This level was chosen in order to accommodate rather deep devices such as the streak camera. This 8 inch elevation is within the range of standard ½ inch posts and post holders, which apparently come in off-the-shelf lengths of 3, 4, and 6 inches.

The table will be supported by four independent “legs” with no cross bracing between them. If one were to follow the APS example, the legs would contain no special provision for vibration isolation of the table from the floor. All legs have a natural resonant frequency, and non-isolating legs resonate at roughly 35 Hz or so. On the other hand, pneumatically damped isolators have a natural frequency of roughly 2 Hz. Assuming that ambient floor vibrations are insignificant (the

experimental results are still being evaluated), we are not convinced the same can be said for the floor vibrations induced by the rolling motion of the massive concrete radiation doors situated near the end station. Although their motion is expected to be infrequent, it could jeopardize the optical alignment of the OSR line.

## 2.12 OSR INSTRUMENTATION: PHASE I

We have already discussed the instrumentation priorities in general terms. Implementation is proposed in two phases, and here we will focus on Phase I, which includes the essential instrumentation for the early stage of the storage ring commissioning.

Since the beam intensity will vary a great deal during commissioning, it will be useful to establish some reference “benchmarks” for the photon input to the OSR detectors. Our reference parameters are as follows:

- Beam current 100 mA
- Ring frequency 1.75 MHz
- Bunches per turn: 204
- Photon wavelength  $\lambda = 550$  nm
- Acceptance bandwidth  $\Delta\lambda = 6$  nm (1%)
- Angular acceptance (horizontal)  $\theta_h = 1$  mrad

For this multibunch mode, the corresponding photon flux is

$$I = 2.8 \times 10^4 \text{ photons/mrad/bunch}$$

or

$$I = 5.6 \times 10^6 \text{ photons/mrad/turn}$$

where the time for 1 turn is 570 ns.

For a single-bunch mode of operation and an average current of 5 mA, the single-bunch flux is

$$I = 2.8 \times 10^5 \text{ photons/mrad}$$

within the same bandwidth as above (1%). As noted elsewhere, the actual horizontal angular acceptance will typically be  $\theta_h = 4$  mrad, and a bandwidth of 5% is an option, amplifying the above intensities by a factor of 20.

Very low current studies at the level of a few mA or less entail photon fluxes of the order of  $10^3$  photons per bunch. This roughly defines the required lower limit of imaging sensitivity of the instrumentation for fast temporal studies.

The proposed Phase I detectors are discussed below. The primary image, as projected by the relay lens system from the source point, will be focused about 0.5 m in from the entrance to the optical table, and beam splitters will distribute the light to the various detector stations. *The primary image will be relayed to each detector by secondary lenses, which may also act as image magnifiers.*

A proposed layout of the six detectors (Phase I and Phase II) on the optical table is illustrated in Fig. 2. Given N devices, we require N-1 beam splitters. The arrangement shown minimizes the number of beam splitters on the high-resolution camera lines.

### 2.12.1 Intensified Gated Charge-Coupled Detector Camera.

The ICCD camera has the highest priority. The technology of these devices has advanced to the point where turn-by-turn, and even bunch-by-bunch information can be gathered. The instrument we have in mind (the 4 PICOS) is made by Stanford Computer Optics. It has a 200 ps shutter (gate) and can operate in a 2 MHz burst mode. The burst mode frequency is high enough for us to profile vertical beam-blowups on a turn-by-turn basis (1.75 MHz), and thus to quantify the actual temporal development of the x-y coupling (here we take advantage of the fact that  $\beta_y$  is large at the dipole source point). Others have used these high-speed gated cameras to monitor the vertical beam size on a bunch-by-bunch basis, showing blowup is a function of bunch number. But perhaps the most useful application, especially during the commissioning phase, would be transverse motion studies on a turn-by-turn basis, over several betatron oscillation periods. Our choice of camera is suited for this: pixel size is below 10 x 10  $\mu\text{m}$ , and delay times between subsequent "exposures" can be fine-tuned at the 100 ps level.

On the software side, our immediate priority is to convert the imaging data into first and second moments of the beam profile (i.e. beam centroid and width). A software package is available from SCO, which might meet our requirements ("4 Spec"). An interesting alternative package is supplied by Spiricon Laser Beam Diagnostics, which has been adopted by other synchrotron facilities, and we have been told, is quite "user friendly".

Since the pixel size in our camera of choice is roughly 10 x 10  $\mu\text{m}$ , and the focal plane is roughly 600 by 600 pixels in size, measurement of the beam first and second moments would improve by magnifying the source-point image beyond unity. If the beam is a few hundred microns across, the camera can accommodate magnifications of 5-10; however, similar microscope magnifications at the other facilities have demonstrated problems in the ability to locate the image in the first place. Conclusion: A variable microscope is the ideal option. A low magnification, say 1:1, would locate the image. One could then increase the magnification; say to 4:1, for image analysis. The layout in Fig. 2 shows both options, achieved by lenses that can be inserted into the optical line. Alternative optics are being explored.

## 2.12.2 Ungated Charge-Coupled Camera

This camera is a simple “watch-dog”, monitoring the beam on a multiturn basis, and as such could be useful to the machine operators. It has been positioned on the optical line feeding the streak camera for a reason: it will assist in optimizing the focusing of the source-point image onto the input optics of the streak camera, given that the image is split by a judicious location of the beam splitter.

## 2.12.3 MCP-Intensified Photomultiplier Tube; Avalanche Photodiode Detector

The MCP-intensified PMT has a large dynamic range ( $10^6$ ), which lends itself nicely to a number of applications:

- Determine the stored beam lifetimes at very low beam currents (for example, during the storage ring commissioning phase). At the level of a milliamp or less, the conventional current transformer (DCCT) will not be very effective for this purpose.
- Determine the ratio of bunch populations between two neighboring bunches. The obvious application would be in the so-called single bunch (or few bunch) mode where the electron population of the “empty” satellite buckets should not exceed  $10^{-6}$  of the primary bunch. This scheme, implemented at the ESRF, attenuates the incident light to the level of a single photon per 10 turns, and a few minutes are sufficient to yield a dynamic range of  $10^6$ .
- Determine the circulating beam energy by employing the method of Resonant Depolarization. Through the Sokolov-Ternov effect, electrons in the storage ring become polarized with their spins anti-parallel to the dipole field. In principle, the polarization can approach 92%. Now, the spin precession frequency is directly proportional to the revolution frequency, *which is known very accurately*. An oscillating EM field at the precession frequency will destroy the polarization. The key here is that the beam lifetime is a function of the electron polarization. At the correct oscillating EM frequency, a sudden drop in lifetime will be noted. The change is very small, so an accurate lifetime measurement is required, a nice application for the MCP-PMT.

A commercial instrument that meets our criteria is the Hamamatsu model R5916U-50. The advantage is that this model is gateable, with a gate down to 5 ns. Avtech (of Canada) markets a pulser that can gate this device, a combination that has worked nicely at the ALS. The rise time is fast, 180 ps, and the pulse width is 350 ps. Finally, the photo cathode diameter is 10 mm, a real advantage when it comes to capturing the OSR.

The disadvantages of this unit are its rather high price (over \$20, 000 U.S.), and the extreme care required to avoid damaging it through, for example, excessive light or mechanical shock.

An alternative instrument that also meets most of our criteria is the Avalancher Photodiode Detector (APD), which is in use, for example, at the APS. Hamamatsu APD type numbers S2381 and S6045-01 are representative: spectral response is 400-1000 nm, peaking at 800 nm, and the cut-off frequency is 1000 MHz. The problem with these detectors is that the spectral response is reduced by a factor of 3-5 if we operate near  $\lambda = 550$  nm. Furthermore, the active detector diameter is only 0.2 mm, which greatly complicates the optical coupling and alignment. A moveable stage would be required to fine-tune the alignment. Although much cheaper than the MCP-PMT, the APD option is still under review. For example, detector models are available with active detector diameters of 1 mm, but the cut-off frequency is reduced to 600 MHz. Unfortunately, detectors peaking at  $\lambda \approx 600$  nm have much lower cut-off frequencies (250 MHz).

### 2.12.4 Position Detector

A stand-alone beam position detector, which is sensitive to the beam centroid position, is best achieved by commercial analogue (versus pixal) devices. Hamamatsu provides various models of analogue position-sensitive detectors (PSD's) based on analogue readouts along the top and bottom edges. Position resolution is roughly 1-2 microns. Such a device might be useful in resolving the question of beam motion: machine or user I.D. driven?

### 2.12.5 Fast Photodiode; Sampling Optical Oscilloscope

The detectors described above are designed to measure the beam transverse phase-space distributions. Longitudinal phase-space distributions require very fast cameras, since the bunch length (damped) is of the order 50-60 ps. This is the natural domain for the (expensive) streak cameras, with resolutions of 2 ps or less. While the streak camera will be an eventual reality here, an interim bunch-length measurement capability may be desired, even if rather crude.

The fastest photodiode detector on the market at this writing is the PX-D7 marketed by Newport, which has an impulse response time of 7 ps. Conversion gain is about 1.7 V/W, so for an input sync light power of about 100 milliwatts (peak, not average, which we expect for a 200 mA beam and a 4 mrad horizontal acceptance), the output signal is hundreds of millivolts, certainly adequate. However, the active diameter of the detector is only 50  $\mu\text{m}$  and optical coupling must be considered carefully.

We have found only one other facility that actually uses this particular detector for bunch-length measurements, namely the Brazilian light source at Campinas (LNLS), and our discussions with

them have been encouraging. The optical coupling is made at LNLS through a mono-mode optical fiber, with light focusing from a 40 mm diameter, 120 mm focal length lens. The optical situation at CLS needs further study, if this particular fast photodiode option is to be considered further.

The fast photodiode signal needs to be captured by a digitizing oscilloscope if single-turn capability is to be realized. Bandwidths of 20 GHz are readily available, but are marginal for our application. We note that HP has recently introduced a 50 GHz model with a transition time (10% to 90%) of about 7 ps, nearly commensurate with the speed of the photodiode.

A possible alternative to the Fast Photodiode for bunch length measurements, discussed above, is a Sampling Optical Oscilloscope. Such a device has been introduced by Hamamatsu in various models. The model C8188-01 comes closest to our requirements. Basically, the instrument is a slower (and cheaper) version of a streak camera, with a response characteristic of 20 ps and a bandwidth of 20 GHz or more.

The aperture is 100  $\mu\text{m}$  x 3 mm (fixed slit), larger than the Newport fast photodiode. The sampling interval can be as small as 2.5 ps. However, a sampling scope certainly precludes single-turn bunch measurements. Bunch length observations will thus be an average measure that includes the effective spreading due to longitudinal oscillations. This is useful information of course; it would be doubly useful if supported by single-turn bunch length measurements from the fast photodiode.

## 2.13 OSR INSTRUMENTATION: PHASE II

The instrumentation of Phase I is not capable of providing definitive measurements of the beam emittance, bunch length (and phase), beam instabilities, etc. These beam characteristics will be more precisely determined by the Phase II instrumentation, to be installed at a later date. These devices will be essential for fine-tuning the storage ring towards its ultimate design objectives.

Phase II will consist of two principle instruments: a streak camera for the OSR beam line, and a pinhole camera (the "camera obscura" of earlier times) to be situated on the XSR beamline. *The XSR line will be discussed in a later section*, so our comments here are reserved for the streak camera.

The particular streak camera in use at several facilities is the Hamamatsu model C5680 which has a temporal resolution of 2 ps or better, thus permitting a study of the transient beam structure on a bunch by bunch basis. Depending on the various sweep options and camera orientation, one can photograph a single bunch, or a bunch train, *from either the front, the top, or the side*. The front view, also called the *focus mode*, is made with the fast sweep turned off. Extreme caution is required in this mode since the high flux density can destroy the micro-channel plate

amplifier. The top and side views are readily accommodated by means of a Dove prism. This totally-reflecting prism, when rotated  $45^\circ$  about its axis, rotates the outgoing light by  $90^\circ$ . When the prism is not inserted in the optical line, the streak camera provides a top view of the bunch. With the Dove prism inserted, we gain a side view of the bunch.

The basic options for this particular camera include the synchroscan module (M5675) and the dual time base extender (M5679). The former lets one lock on to a given bunch sequence *with very little timing jitter* (compared to the jitter in the single-shot option). However, the present synchroscan frequency range is 75-165 MHz, which means that with the CLS RF frequency of 500 MHz, we can capture only one bunch in four in immediate succession. Actually, by recording an image on the fly-back, we can reduce the capture to one bunch in every two in immediate succession. The dual time base extender provides an orthogonal sweep that permits a temporal separation of the bunch images, *in effect laying down bunch images side-by-side*. As others have demonstrated, this is a powerful tool for examining the onset of longitudinal instabilities and transverse head-tail instabilities. Synchroscan timing comes from the master RF oscillator. Even so, we note that the RF signal at the ALS facility is filtered through a cavity ( $Q = 1000$ ) to reduce the timing jitter. Something to keep in mind.

The streak camera is a very expensive precision instrument that is easily damaged if subjected to an optical overload, so light control through the appropriate filter needs to be considered carefully.

The Hamamatsu camera comes with a standard front-end optical package. The camera is so fast that one must consider the time-delay effects of chromatic dispersion in the front-end optics (roughly 0.1 ps per nm at 500 nm). A narrow bandpass filter, of say 1–5% bandpass, is therefore essential for optimal resolution.

We have queried Hamamatsu concerning the number of photons required to image a single bunch in a single-shot streak. They provided the following ballpark estimate: for a single 100 ps pulse at 500 nm and an image spot size of  $70\ \mu\text{m}$ , *a minimum of 1600 photons is required* at a 1 ns sweep (this assumes a 5% quantum efficiency, and 10 ps resolution).

Let us put this within the context of the OSR photon budget, assuming a beam current of 100 mA and a multibunch mode. Two beam splitters divide the light before the camera, dropping the intensity by a factor of four. The filter bandwidth will be taken as 5% and the full angular acceptance  $\theta_n = 4\ \text{mrad}$  is assumed. From the flux presented in Sect. 2.12, the photon intensity at the streak camera is roughly  $1.4 \times 10^5$  per bunch. Although this appears to be adequate, it is contingent on squeezing all photons through the camera entrance slit of dimensions  $150\ \mu\text{m} \times 3\ \text{mm}$  (H x W). An extra demagnifying lens will probably be required (not shown in Fig. 2).

Concerning the software analysis, we note that the Hamamatsu system includes an analysis package called HPD-TA (High-Performance Digital Temporal Analyzer), but so far we have heard no comment from our colleagues on the performance characteristics of the package.

## 2.14 OPTICAL PULSE-LENGTH WITH A FINITE APERTURE

If we wish to use the OSR to measure bunch lengths, then it is necessary that the duration of the light flash from a zero-length bunch of electrons, emanating from our dipole source-point, be much less than from a typical realistic bunch, of length in the 50-60 ps range.

First, suppose the angular acceptance of the optical system observing the light is *infinitesimal*. We are observing light emitted along an arc, but we only detect the whole arc (of angular extent  $2/\gamma$ ) as a consequence of the  $1/\gamma$  opening angle of the radiation, relative to the electron trajectory. As the text books report, the time duration of the flash is approximately

$$\Delta t = \frac{4r}{3c\gamma^3}$$

where  $\rho$  is the dipole magnet radius-of-curvature, and  $\gamma = E/mc^2$  as usual. For our situation, this gives  $\Delta t \approx 10^{-19}$ s.

Now let us open up the angular acceptance to a total fan width of  $\theta$ , and let us assume  $\theta \gg 1/\gamma$  (true if  $\theta = 4$  mrad as previously suggested). The observable electron-beam arc-length is given by  $\ell = r\theta$ , so the transit time of the electrons along our visible arc is  $\delta t = \rho\theta/c$ , *which common sense would dictate to be the flash duration*, and which has been so-stated in the literature.

Again, for our situation this gives  $\delta t = 93$  ps, much longer than the actual bunch lengths. Fortunately, *the argument is false*, and is our reason for raising the issue here. The argument does not compensate for the flight time of the photons emitted at the beginning of the arc (the electrons are moving at nearly the speed of light). Our analysis (for  $\theta \gg 1/\gamma$ ) gives

$$\Delta t = \frac{r\theta^3}{12c}$$

or  $\Delta t \approx 10^{-16}$ s. Conclusion: the finite angular acceptance of the optical system has little effect on the resolution of the bunch length as determined by our instrumentation, at least insofar as the observable arc-length is concerned.

## 2.15 FOCUSING AND CALIBRATION

It is proposed to eventually install six measuring instruments on the end-station optical table. The disposition of these devices is portrayed in Fig. 2. As noted, first priority is assigned to the CCD

and ICCD cameras. The focal points of the primary and relay lenses are indicated by x's in the figure, starting with the primary-lens focal points situated just following the beam splitter near the table entrance.

Two issues need to be addressed. The first is how to establish the principle focal points, and subsequently the focal points of the relay lenses. The second issue concerns determination of the image magnification from the source point to the detector, and how to extract the image size from the detector response (pixel size, etc.). The two issues we characterize respectively as "Focusing" and "Calibration". Let us state at the outset that, so far, we do not have a definitive solution for either issue. Various options as explored by other facilities are found in the literature, and we summarize them below for possible consideration.

- Calibration. If the focal lengths of the optical elements are well understood, a theoretical calibration can be calculated. An experimental check can be made by shifting the electron beam by a *known amount* vertically and measuring the focused image response. This depends on an accurate knowledge of the local bump system, and an accurate measurement of the change in beam position.
- Calibration (cont'd). We have seen instances where the CCD calibration is made by projecting an "optical marker" (a carefully measured reticle) onto the instrument cathode, through a beam splitter. Presumably the pre-camera optics is calibrated by a theoretical model of the system.
- Focus and calibration (cont'd). Perhaps the most straight forward measure of the system alignment, focus, resolution and magnification is obtained by inserting a retractable reticle at the dipole magnet source point. This has been used successfully at the APS, where the reticle has four 1 mm holes arranged in a 3 x 4 mm rectangle. Unfortunately, from the structure of the dipole vacuum chambers, this does not appear to be a viable option at the CLS.
- Calibration (cont'd). The design report for the ALS includes the following remark: "TV cameras viewing the synchrotron light image against a reference graticule provide a reliable beam position and transverse size diagnostic." A follow up inquiry revealed that the x-ray component was being utilized, with a fluorescent screen situated outside the beryllium window (in air). It was observed by a small TV camera equipped with a microscope lens, since the spot size was only the order of a millimeter in size.
- Calibration (cont'd). The ESRF has developed a calibration procedure that requires further clarification. They state that they "use individual transverse  $\mu$ -metric slides for each of the three components (2 lenses and a CCD camera). Displacing each of

these components represents a transverse source-point displacement of the same value, but of opposite sign....”.

As noted elsewhere, our first priority is to establish the principle focal points of the primary imaging lens. The focal positions are indicated by the pair of x's following the beam splitter, as the light enters the table (Fig. 2). The focus is adjusted by shifting the longitudinal position of the primary lens until a minimal image size occurs. This might be checked, for example, by placing a very thin semi-opaque screen at the  $90^\circ$  focal position following the splitter, and observing the spot with a conventional CCD camera. To remove chromatic aberrations, one needs to install (temporarily) a band-pass filter between the beam splitter and the screen. Also, maximum sensitivity to depth-of-focus will occur when the effective f-stop is a minimum, as defined by the primary slit system.

Once the primary focal points are established, the focal positions of the relay lenses might be similarly established.

The second issue, calibration, remains problematical. It is critical for instrumentation designed to measure spatial characteristics of the stored beam, specifically the ICCD camera and the streak camera. Indeed, one could argue that calibration should take priority over all other considerations, since issues like diffraction limitations carry little weight *unless* the system calibration is understood.

## 3.0 THE XSR BEAMLIN

### 3.1 INTRODUCTION

The XSR beamline will probably be included as part of the Phase II instrumentation, since its small field-of-view only makes it useful once the machine orbit has been stabilized. The XSR line basically consists of a source-point in dipole-2, an adjustable rectangular pinhole aperture (0-100  $\mu\text{m}$ ), and a CCD camera. From the experience of other facilities, the source-to-image magnification should not be less than unity. Therefore, we have situated the pinhole within the shielding tunnel. The source to pinhole distance is about 8 m, and the pinhole to camera distance is about 12 m, yielding a magnification of 1.5.

By its nature, the pinhole camera is aberration-free and achromatic. Since the angular acceptance of the slit system is roughly 3  $\mu\text{rad}$ , the curvature limit [Eq. (7)] and the depth of field limit [Eq. (11)] are negligible. The intrinsic diffraction limit due to the radiation opening angle *at the source* [Eq. (9)] is likewise negligible.

The main function of the XSR line is to determine the electron beam size at the source point in order to deduce the beam emittance and x-y coupling. The crucial optical issues are

- i. Can the camera see the *total* vertical and horizontal spatial extents of the beam?
- ii. What is the spatial resolution of the camera *at the source point*?

The first issue is strongly dependent on the machine Twiss parameters at the source point. The second issue depends on a trade-off between geometric and diffraction optics. Both issues are addressed later.

### 3.2 FRONT END AND THE POWER DENSITY

As noted elsewhere, at 500 mA the total radiation power from the dipole source-point is 70 Watts/mrad, integrated over the vertical angle. Since the power is concentrated in the x-ray region, the total vertical opening angle is roughly 0.3 mrad ( $\pm 2\sigma$ ) [Eq. (13b)]. The high power in the x-ray region was subdued in the OSR line by introducing an optical chicane, but here it is precisely the hot x-ray fan we wish to utilize. Thus, unlike the OSR line, safety issues demand that the XSR line incorporate a “front end” structure that, among other things, protects the subsequent hardware from possible missteering of the electron beam. Human safety issues are also a factor to consider on x-ray lines, but the tiny flux through the pinhole slit (located inside the tunnel) considerably reduces the level of radiation in the end-station, as compared for example to the more conventional x-ray beam lines. Nevertheless, for economical reasons it makes sense for us to employ one of the common designs developed for the CLS front ends.

Front ends for dipole source-points are classified as BM1 or BM2, depending on whether the source-point is within the first or second dipole of each of the double-bend achromat cells. The XSR line is anchored on BM2. The standard front end for a BM2 is over 6 m long, longer than we can accommodate if the pinhole is situated within the tunnel. *So we will adopt the much shorter (roughly 4.8 m) BM1 front end to our BM2 line.* The BM1 front end dispenses with the acoustical delay line (designed to disperse the acoustic shock wave in the event of a window failure.)

The BM1 front end incorporates two photon beam position monitors, to define the beam position and angle. Although the foreshortened BM1 geometry reduces the angular accuracy, nevertheless the position monitors may prove useful in aligning the XSR beamline.

### 3.3 EXIT WINDOW

The standard exit window for the front ends incorporates beryllium in a double-wall arrangement with radial cooling, in accordance with the CLS vacuum policy. The diameter can be small since

the subsequent pinhole aperture is sub-millimeter in size. The beryllium window has both positive and negative consequences for the x-ray beam.

- On the positive side, the window acts as an optical filter, removing the long wavelength components, which improves the diffraction-limited spatial resolution of the pinhole camera. Thus, total beryllium window thickness of 10  $\mu\text{m}$ , 100  $\mu\text{m}$  and 1000  $\mu\text{m}$  in effect remove photons below 1000 eV, 2000 eV and 3000 eV respectively. Photon transmission is 90% or greater for energies above 2000 eV, 4000 eV and 10,000 eV respectively, for the three window thicknesses. For reference, the critical energy of the facility is about 7000 eV.
- On the negative side, photon scattering by the window in effect increases the emittance of the x-ray beam and hence increases the image size at the detector. This is difficult to quantify in the absence of experimental data. We note that Rayleigh scattering is the dominant process, and at 1-10 keV photon energy is mildly, *but not strongly*, forward-peaked in angular distribution, thus generating a “gentle” halo around the central image. A significant deterioration of the image requires the contribution of a strongly forward-peaked scattering process (like the Mott scattering of electrons by atomic nuclei), but we are not cognizant of any such process for photon scattering.

Conclusion: All things considered, one should minimize the thickness of the beryllium windows (certainly well below 1mm each in the double-window arrangement), and provide any necessary optical filtering near the detector station.

Although beryllium windows will be a factor during the early stages of operation, the longer term plan is to dispense with them altogether and run a continuous vacuum line from source point to near the detector. This will require differential pumping, and so the beamline will be designed from the beginning in order to accommodate the windowless operation. (An exit window near the detector will likely still be required, but here the scattering effects are negligible.)

### 3.4 PINHOLE SLITS

The power density parameters described in Sect. 3.2 translate into a heat load of about 4 Watts/mm<sup>2</sup> at the pinhole location. In order to limit the power load on the pinhole slits, a water-cooled pre-collimator of diameter 1-2 mm is required. The resulting power load on the pinhole is then roughly 4-16 Watts. Although this load is small, the accumulative effect over time, an hour for example, *might* lead to thermal expansion of components that modify the aperture by several microns, which for a total aperture of 20-50  $\mu\text{m}$ , is not acceptable. The problem needs to be studied in detail to determine if water cooling of the pinhole is required, or whether air flow is

sufficient. Note that the pinhole may be situated either in vacuum, or within a helium environment (below).

It makes sense to adopt the pinhole design of a proven system, and the APS diagnostic beamline is a good model. The pinhole slits there are fabricated from 6 mm thick tungsten (99.5% pure), and the collimating surface of each jaw is ground on a circle of radius 50 mm, as seen by the beam. This greatly eases the mechanical alignment tolerances compared to the conventional square-jaw configuration. The APS pinhole system is water-cooled, with temperature regulation to within  $\pm 0.05^\circ$  C. (The APS experience with air-cooled slits was unsatisfactory.)

Mechanically, the four jaws of the pinhole slit system must be individually driven by actuators capable of providing a pinhole aperture (x and y) in the 0-100  $\mu$ m range. Resolution on the jaw position, and in particular the position reproducibility, must be in the micron range, all by remote control and with remote position readout.

Global alignment of the slit system is a separate issue. If the XSR optical table is firmly anchored (as in the APS diagnostic lines), then a separate motor-driven global alignment mechanism for the slits might be an option. The alternative is to have a large (several mm) motion ability on each of the pinhole jaws in order to center the system over a range of several mm.

A few companies supply x-ray slit systems on a commercial basis. One system that comes closest to matching our specifications is supplied by Advanced Design Consulting. The whole package, including the control system, is priced at \$ 6800 U.S. Once could not begin to design a home-made system for this. There are, however, two outstanding issues concerning this product: heat dissipation (there are no cooling arrangements), and overall alignment (the slits are beveled at  $0.5^\circ$ , which therefore defines the alignment tolerance).

Finally, we note that there is a significant advantage to having the pre-collimator designed as a sort of high-power version of the pinhole slit system (i.e. variable aperture with independent jaw control), rather than as a fixed-aperture device. The major advantages hinge on alignment with respect to the x-ray centerline, and a sub-millimeter aperture to further reduce the pinhole heat load.

### **3.5 TRANSFER LINE**

The x-ray transfer line from the beryllium window system to the optical table must be an enclosed line, either a vacuum line or a helium channel.

A 12 m helium channel at STP has an area density of  $0.2 \text{ gm/cm}^2$ , equivalent to a beryllium foil 1 mm thick. We have suggested that such a foil thickness may be problematical as far as multiple scattering is concerned, and certainly the scattering effect of the channel must be designed to be less than that of the windows. Since 1 mm of beryllium is rather excessive, a

*helium channel should operate at a pressure of something lower than 0.1 atmosphere.* Studies show that a helium channel at STP results in strong photon absorption below 2 keV, although the transmission for energies above 6 keV is about 96%.

Alternatively, if we employ a vacuum channel, the absorption property of air would require a residual pressure much less than 0.1 atmosphere, although a high vacuum is not necessary. A modest vacuum of 10 millitorr yields a transmission in excess of 99% for photons above 2 keV.

In either case, it will be necessary to terminate the transfer line with a thin beryllium window near the imaging system.

### 3.6 IMAGING SYSTEM

The x-rays emerge from the transfer line through a thin window (beryllium) and are converted to visible light ( $\lambda = 530$  nm) by a thin YAG crystal. The converter must be very thin to minimize image distortion (blurring) due to internal rescattering within the crystal. The image formed within the converter is observed by a detector consisting of a magnifying device followed by a CCD camera. Between the converter crystal and the camera is some mechanism for controlling the light intensity entering the CCD camera.

- Window-to-converter air gap. We note that the x-ray attenuation by 1 mm of beryllium in the 2-10 keV region is commensurate with the absorption properties of 10 cm of air at STP. Thus, the air gap between the exit window of the transfer channel and the YAG converter is certainly a factor to be considered in the optical response of the XSR beamline, as defined by the Point Spread Function and the Modulation Transfer Function, defined below. *The transition gap should be kept to an absolute minimum.*
- YAG x-ray converter. Commercial crystals of thickness in the 100-200  $\mu\text{m}$  range are available, without requiring an underlying substrate for stability. Thinner crystals are difficult. Converter thicknesses run from about 100  $\mu\text{m}$  (APS) to 500  $\mu\text{m}$  (NSLS).
- Magnifying device. Since the CCD camera pixel size is the order of 10  $\mu\text{m}$  x 10  $\mu\text{m}$ , and the primary source (beam) size is roughly 340  $\mu\text{m}$  wide and 130  $\mu\text{m}$  high [recall Eqs. (5)-(6)], beam profile measurements will benefit from even modest magnifications (2-4) between the converter and camera. The APS uses two achromat combinations, each with an infinite conjugate ratio, to accomplish the magnification. Their argument is that aperture-control between the lenses is simplified, thus minimizing image distortion. A simpler option adopted by the NSLS employs a commercial 50 mm focal length Nikon lens connected by a bellows to the CCD camera. The lens is positioned to give a factor of 2.4 magnification. Greater

magnifications are accomplished with commercial lenses of longer focal lengths. The optical system at Spear 2 apparently utilized 3 lenses (Nikon) providing magnifications of 1, 3 and 5.

- Aperture control. While still on the subject of light control, let us note the options for adjusting the intensity of light falling on the CCD camera.
  - i. Attenuator wedge in the x-ray line. Several facilities insert a copper wedge to control the x-ray flux, but the APS rejects this option since they argue that it introduces small-angle scattering into the photon beam.
  - ii. Neutral-density filters. Inserting ND filters following the YAG converter is an option, but again the APS experience has been negative, due to curvature in the filter surface, and also tapered thickness in the filter. Their conclusion: fixed apertures are more reliable than the above options.
  - iii. Fixed or variable apertures. An f-stop control following the YAG converter is the best option, and to avoid a complicated control system, a diaphragm control *independent of the lens system* is preferred. In other words, we propose an iris system similar to that employed in camera systems, but in a stand-alone mode following the YAG converter.
- Mirror. As part of the above imaging system, it is necessary to deflect the optical light (following the YAG converter), through an angle of  $90^\circ$ , into the CCD camera. This is necessary to remove the camera from the forward-flux of x-rays that could damage the camera in the long term.
- Camera. There are several CCD cameras on the market that can serve our purpose (Sony, Cohu, etc), with various trigger options. As to the triggering possibilities, we note the following, which have worked for other facilities:
  - i. T.V. mode (30 frames/sec). This is the most straight forward mode, when time resolution is not an issue.
  - ii. Slow-gated mode. Most CCD cameras permit “slow” gated operation, where integration times can be controlled within the range 0.1–20.0 ms, which is commensurate with the transverse and longitudinal damping times (2-4 ms).
  - iii. Fast-gated mode. Fast gating, sufficient for example to resolve individual bunches, can be achieved by utilizing a fast-gated micro-channel plate image intensifier (MCP) in concert with a conventional CCD camera, similar to the OSR arrangement described in Sect. 2.12.1. Here, however, we are limited by the YAG converter decay time-constant, about 70 ns, as compared with the storage ring bunch circulation time of 570 ns. Thus, although capable of

a single-bunch analysis (for example), the scheme can not analyze adjacent or consecutive bunches.

- Beam diagnostic control and software. A popular frame grabber and software package for gating, digitizing, and controlling the image integration time of CCD cameras in the 30-1000 pulse-rate range is provided by Spiricon (distributed by Optikon in Canada). Originally designed for laser beam diagnostics, it has been employed at several synchrotron facilities for the profile analysis of both visible and x-ray (converted) light. These facilities include the ALS, the NSLS, the APS, and SPEAR2. Among other things, the package provides both a visual and quantitative description of the converted x-ray beam profile, suitable for further analysis. This software package was previously mentioned in connection with the OSR line, in Sect. 2.12.1
- Floating platform. The entire Imaging System, consisting of the YAG crystal x-ray converter, magnifying device, aperture-control iris system, deflecting mirror, and the CCD camera, should be mounted on a common x-z translation stage, with prealigned optics. The XSR aperture is very small, making individual alignments difficult. This prealigned concept has worked elsewhere (ESRF for example). The resolution of the lift stage is decided by the absolute positional accuracy required of the pinhole slits system. *We suggest that lifter-resolution at the micron level is required.*

### 3.7 EMITTANCE MEASUREMENT

In this section we address the issue of emittance measurement of the storage ring electron beam using the XSR beamline. In the next section we will discuss the limits to the spatial resolution at the source point, as determined by geometric and diffraction optics. Both sections are relevant to the measurement of the beam size in both planes, and together they constrain the ability of the XSR beamline to determine the x-y coupling in the storage ring. Of course, the XSR beamline has applications other than emittance and coupling measurements. For example, its small angular acceptance makes it a rather good photon position sensor, which might be useful to the User Community.

We turn first to those particular theoretical issues which reflect directly on the algorithm for deducing the emittance of the electron beam *in both planes*. Now, as is well known, the vertical beam emittance  $\epsilon$  can be deduced from a measurement of the beam size through the relation

$$y = \sqrt{\beta \epsilon} \quad (14)$$

where  $\beta$  is the usual Twiss parameter at the source point, and  $y$  is the *actual* beam radius (at the one- $\sigma$  level). The question is, do the XSR measurements provide a true determination of the

beam size? In general, the answer is “no”, and one can not then employ Eq. (14), at least in the vertical plane as discussed below. Before engaging in the details, let us skip to the bottom line and state that, for the CLS, the above simplistic relation [Eq. (14)] is actually a pretty good approximation for our purpose, where  $y$  is the *observed* beam size. Let us now focus on the vertical emittance, after which we will consider the rather different constraints on the horizontal measurements.

### 3.7.1 Vertical Electron Emittance

In order to appreciate the limitations of Eq. (14) in general, it is necessary to distinguish between the *actual* electron beam radius  $y$ , and the radius as *perceived* by the pinhole camera. They are not necessarily the same. The distinction is best understood in phase space, and for reasons that will become evident later, we will confine our argument to the vertical, or  $(y, y')$ , phase space.

In the  $(y, y')$  phase space, the trajectory (acceptance) of the pinhole aperture is a straight path described by the equation  $y' = -y/L_1$  where  $L_1$  is the distance from the source to the slit. We neglect the actual slit width here.

Of interest is how the above tilted-but-linear phase space acceptance intercepts the  $(y, y')$  phase space ellipse of the photon beam. For the moment we ignore the photon opening angle, so the photon and electron phase spaces are identical. Picture an electron phase space ellipse at the source point which, for arguments' sake, happens to be “tilted” (i.e. the Twiss parameter  $\alpha_y$  is large). Our linear acceptance function slashes across the ellipse, and the line-ellipse intercept-points, as projected on to the  $y$ -axis, express the beam size *as perceived by the XSR system*. However, the actual beam size is given by the *extreme*  $y$ -projections of the beam ellipse [Eq. (14)] which could (in principle) be larger than the above intercepts. These issues are illustrated by Fig. 3a and Fig. 3b, where the line represents the pinhole phase-space trajectory, and the inner ellipse describes the electron (photon) phase space. In both examples, the perceived beam size is clearly much smaller than the actual size. To summarize, the perceived beam size could be somewhat smaller than the real beam size and Eq. (14) can not then be used. Note, however, that everything is easily resolved if the beam phase space ellipse is “upright”, or nearly so, at the source point. For reference, the above issues are discussed in detail in the articles by Safranek (EPAC '96) and Limborg (EPAC'00).

In our discussion so far, we have ignored the finite opening angle of the photons with respect to the electron direction, and as we shall see, this can change everything. The opening angle merely serves to expand the electron phase space ellipse along the  $y'$  direction, but of course has no effect along the  $y$ -axis. This expanded ellipse defines the photon phase space, which is what

we measure, and is somehow to be connected to the electron beam emittance. In Fig. 3a and Fig. 3b, the photon phase space now becomes the outer ellipse in each case.

Still in the vertical ( $y, y'$ ) plane, it becomes clear that extracting the vertical emittance of the electron beam from a *tilted photon ellipse* is not trivial in general, and we direct the reader to the comprehensive article on the subject by Elleaume, J. Synchrotron Rad. (1995) p.209. In the general case, all of the Twiss parameters are required to untangle the emittance from the measured quantities.

Happily, the XSR source point parameters of Eq. (2) for the y-plane are favorable to the simple size-vs-emittance relation of Eq. (14), and indeed we actually benefit from the fact that the electron ellipse is quite strongly tilted in phase space. Figs. 3a and 3b have been calculated for our source-point parameters and for a horizontal electron emittance  $\epsilon_x = 18.2 \text{ nm} - \text{rad}$ . The two figures correspond to x-y coupling of 1% and 10%, respectively. The opening angle ( $1\sigma$ ) is given by Eq. (13b). We see in Fig. 3a that the pinhole trajectory (straight line) intercepts the photon ellipse quite close to the y-extremes of the electron ellipse, and thus gives a good measure of the electron beam size. The situation gets even better for smaller x-y couplings. On the other hand, Fig. 3b demonstrates a breakdown of our simple model when the coupling gets large.

In conclusion, for x-y couplings less than about 5%, the simple relation Eq. (14) is adequate for our purpose, *where y is the perceived radius of the photon as deduced by the XSR pinhole camera.*

### 3.7.2 Horizontal Electron Emittance

The situation in the horizontal plane is somewhat different. In the first place, the half-width of the beam must be augmented by the finite energy spread of the beam ( $\pm\delta$ ) in conjunction with the dispersion function  $\eta$ , so that Eq. (14) in the horizontal plane becomes

$$x = [\beta\epsilon + (h\delta)^2]^{1/2} \quad (15)$$

where  $\beta$  and  $\epsilon$  are the horizontal  $\beta$ -function at the source point, and the horizontal emittance, respectively.

Secondly, the line-ellipse picture as employed in the ( $y, y'$ ) phase space is altered in the ( $x, x'$ ) phase space. Although the picture is correct at the *instantaneous* level, one must take into account the motion of the electrons along the small circular arc in the dipole, as subtended by the pinhole. The angle-versus-position correlation on the phase space ellipse becomes essentially lost on a time-averaged basis. To understand this, ignore the photon opening angle with respect to the electron direction. Then, as the electrons cross the small arc, the photons sweep like a search light beacon, in effect cutting a large angular swath, with very little change in *apparent*

position. Translated into  $(x, x')$  phase space, the time-averaged phase space path is approximated by lines sweeping along  $x'$ , at roughly constant values of  $x$ . If one now superimposes the pinhole linear phase-space trajectory, the intercepts occur at roughly the maximum extents of  $x$ . *In other words, the perceived maximum dimension in  $x$  will always be close to the beam size, no matter what the "tilt" of the instantaneous phase space ellipse is, so Eq. (15) can always be applied to measure  $e_x$ .*

Conclusion: Both Eq. (14) and Eq. (15) can be applied on the CLS x-ray diagnostic beamline to deduce the electron emittances in both planes, where  $x$  and  $y$  are the *perceived* beam radii.

Corollary: If  $L_1$  and  $L_2$  are the source-pinhole and pinhole-image distances, then the XSR beamline magnification indeed is  $L_2/L_1$  in both planes (in the general case, this is not necessarily a correct statement).

Summary: The connection between the measured photon beam parameters (size, divergence) and the electron beam emittance in general is a function of the Twiss parameters at the source point. In certain situations, ours being one, knowledge of the preceding permits a measurement of the electron beam emittance solely from a measure of the photon beam size without a measure of the photon divergence. The vertical emittance of the photon beam is generally much larger than the emittance of the electron beam, due to expansion in the  $y'$  direction from the photon opening angles.

## 3.8 LIMITS TO RESOLUTION

### 3.8.1 Diffraction Limitations

A rule of thumb states that the resolution of an optical system is proportional to  $\lambda^{2/3}$ , where  $\lambda$  is the wavelength of the light, and of course is the argument for using x-rays. The pinhole camera has been described above. In the present section we discuss the limits to resolution of the system as dictated by fundamental geometric and diffraction optics.

The optical response of a system is described by the Point Spread Function (PSF) and the Modulation Transfer Function (MTF). The PSF describes the spatial response to a point source, while the MTF portrays the frequency response (spatial, not temporal). The MTF is essentially the Fourier transform of the PSF. (A more detailed discussion can be found in Smith's "Modern Optical Engineering".) Here, we are going to focus on the PSF of the pinhole system.

Briefly, the issue is as follows. A Gaussian-shaped photon beam impinges on the pinhole aperture, suffers diffraction, and then images on the YAG crystal. If the aperture is large, geometric optics shapes the image (shadow, penumbra, etc.), but if the aperture is very small, we

observe a broad diffraction peak. An intermediate aperture exists where the two effects are in balance to yield the optimum resolution. We use the PSF to search for this optimal configuration.

A correct treatment of the resolution function is based on Fresnel (not Fraunhofer) diffraction. In fact, by adopting the formalism for diffraction as spelled out in "Principles of Optics" by Born and Wolf, both the geometric and diffraction optics are subsumed by a single Fresnel-Kirchhoff integral. The resulting double integral is simplified somewhat by our choice of a rectangular pinhole aperture. Finally, the resulting intensity function is integrated over the energy spectrum of the forward synchrotron light between 5 keV and 30 keV. The spectrum drops very quickly below 5 keV, in part due to the beryllium windows in the beamline front end.

In everything that follows, we will adopt a one-dimensional stance, by setting all initial and final (source point and image point) x-coordinates to zero, within the two dimensional field. Our point source thus devolves solely along the y-axis, and we examine the final image likewise solely along the y-axis. This is sufficient to establish the basic characteristics of the PSF along this vertical cut.

Our computer coding of the F-K integral is instructive in that it clearly demonstrates the gradual transition between geometric optics and diffraction optics as the aperture is decreased. This contrasts with other approaches where one attempts to treat the two phenomena as distinct (for example, see Wilke, B.I.W. '94).

For our definition of "resolution", we adopt the so-called Rayleigh criterion, which roughly translates into the statement that the Gaussian-like images from two point sources should be separated by a distance equivalent to the full-width at half-maximum of each (isolated) image. For a source-slit distance  $L_1 = 8$  m, and a slit-image distance  $L_2 = 12$  m, the following table summarizes our estimate of the vertical resolution of the pinhole camera as a function of the vertical slit aperture.

Aperture ( $\mu\text{m}$ )	Resolution at source ( $\mu\text{m}$ )
50	65
45	55
40	45
35	35
30	30
25	23
20	23
15	30

*Optimal resolution occurs with a slit-width of roughly 25  $\mu\text{m}$ , yielding a resolution of about 23  $\mu\text{m}$  at the source point.* However, this ideal resolution ignores certain instrumental realities, such as the resolution of the YAG-camera combination. The PSF response of the detector system is required in order to properly unfold the observed image of the synchrotron x-rays. The unfolding procedure is best done at the MTF level (i.e. in the frequency domain, rather than in the conventional spatial domain), since the mathematical operation is simple division. But clearly, the whole complex issue of recovering the electron beam profile from the observed patterns in the YAG crystal can not be discussed here, and will be the subject of a separate study.

The optimal ideal resolution for a slit width of 25  $\mu\text{m}$  yields an image at the detector, for a point source, which is very similar to a Gaussian function. This is the idealized Point Source Function, ignoring detector response. Furthermore, recall that the incident x-ray beam itself is roughly Gaussian in cross-sectional profile. The consequences of running a Gaussian function through a Gaussian “filter” is well understood in laser studies: one obtains a Gaussian function at the exit (i.e. the image plane). We will not pursue the issue here, but only note that the diffraction spreading of a Gaussian beam is well understood, and is especially relevant to our application. We refer again to the text by Smith (op.cit.), page 165. Another good reference on Gaussian optics can be found within the on-line catalogue of the optical company Melles-Griot. Indeed, this catalogue includes a veritable on-line textbook on all aspects of optics, presented in a conveniently succinct format.

### 3.8.2 Emittance and Coupling Resolution

The theoretical spatial resolution of the pinhole system is about 23  $\mu\text{m}$  at the source point. This establishes the resolution on the vertical emittance to be about

$$\Delta e_y = 0.060 \text{ nm} - \text{rad.} \quad (16)$$

This translates into a resolution on the x-y coupling of about 0.003 (i.e this is the minimum resolvable coupling). *However, when the other instrumental factors are included, the minimum measurable coupling will likely be about 0.01 or so.*

## 4.0 REPORT SUMMARY

Every extant synchrotron facility has a diagnostic beamline of one form or another. Based on the experience of these facilities, we have proposed an assortment of instrumentation which probes most aspects of the synchrotron physics, including emittance, bunch length, instabilities both longitudinal and transverse, lifetime, insertion device aperture restrictions, x-y coupling, etc. The measurement goals of the instrumentation are fairly modest, insofar as they do not attempt to encompass extremes in beam current (i.e. extremely low or extremely high instantaneous currents), or extremes in the temporal frame (sub-picosecond structures).

The Facility Diagnostic Beamlines (FDB's) consist of the OSR (Optical Synchrotron Radiation) and the XSR (X-ray Synchrotron Radiation) beamlines, which are situated on separate dipole-magnet source points. This separation (a luxury not shared by most other facilities) greatly simplifies the design of the individual beamlines. The OSR line, for example, does not require a "front end" in the conventional sense.

Two phases of installation are proposed. Phase I includes only the subset of OSR instrumentation which is essential for the *initial* commissioning stage of the storage ring. This includes a "wide angle" camera to photograph a potentially erratic beam.

Phase II instrumentation is designed to monitor a "calm" machine, once orbit stability has been achieved. This phase includes installation of a streak camera on the OSR line, and an x-ray pinhole camera on the XSR line.

Finally, we do not wish to exclude more exotic instrumentation designed to address spatial or temporal issues outside our conventional frame. Our particular difficulty at present lies in real estate: how to lay out our conventional instrumentation on the 4 x 8 foot optical table in a manner so as not to preclude easy installation of additional hardware intended for measurement capabilities beyond our original design.

---

## Figure Captions

- Fig. 1 Schematic layout of the OSR beamline optical chicane, showing the primary and secondary mirrors, the aperture slits, and the focusing system.
- Fig. 2 Proposed layout of the detectors on the end-station optical table of the OSR beamline. Six detectors are proposed, as discussed in the text. The x's mark primary and secondary focal positions, starting with the 1:1 image of the source point (the two foci immediately following the first beam splitter). Lenses marked  $M = 1$  and  $M = 4$  provide magnification of 1 and 4 respectively (but not simultaneously). Further options will develop, such as a reducing microscope near the streak camera.
- Fig. 3a Phase space diagram for the XSR beamline in the vertical ( $y$ ) plane, as projected back to the dipole source point. The inner ellipse represents the phase space of the electron beam at the  $1\sigma$  level. The outer ellipse describes the phase space of the synchrotron radiation at about 12 keV, taking into account the photon opening angle ( $1\sigma$ ). The straight line represents the phase-space trajectory as defined by the pinhole camera, assuming a very small aperture. The intercept of the straight line with the photon ellipse defines the maximum extent along the  $y$ -axis actually observed by the camera, here for an  $x$ - $y$  coupling of 1%. Significantly, this extent is close to the actual electron beam size, thus providing a good measure of the latter.
- Fig. 3b This is the same as for Fig. 3a, except here the  $x$ - $y$  coupling is 10%. From the intercepts, it is clear that the perceived electron beam size is much smaller than its actual size.

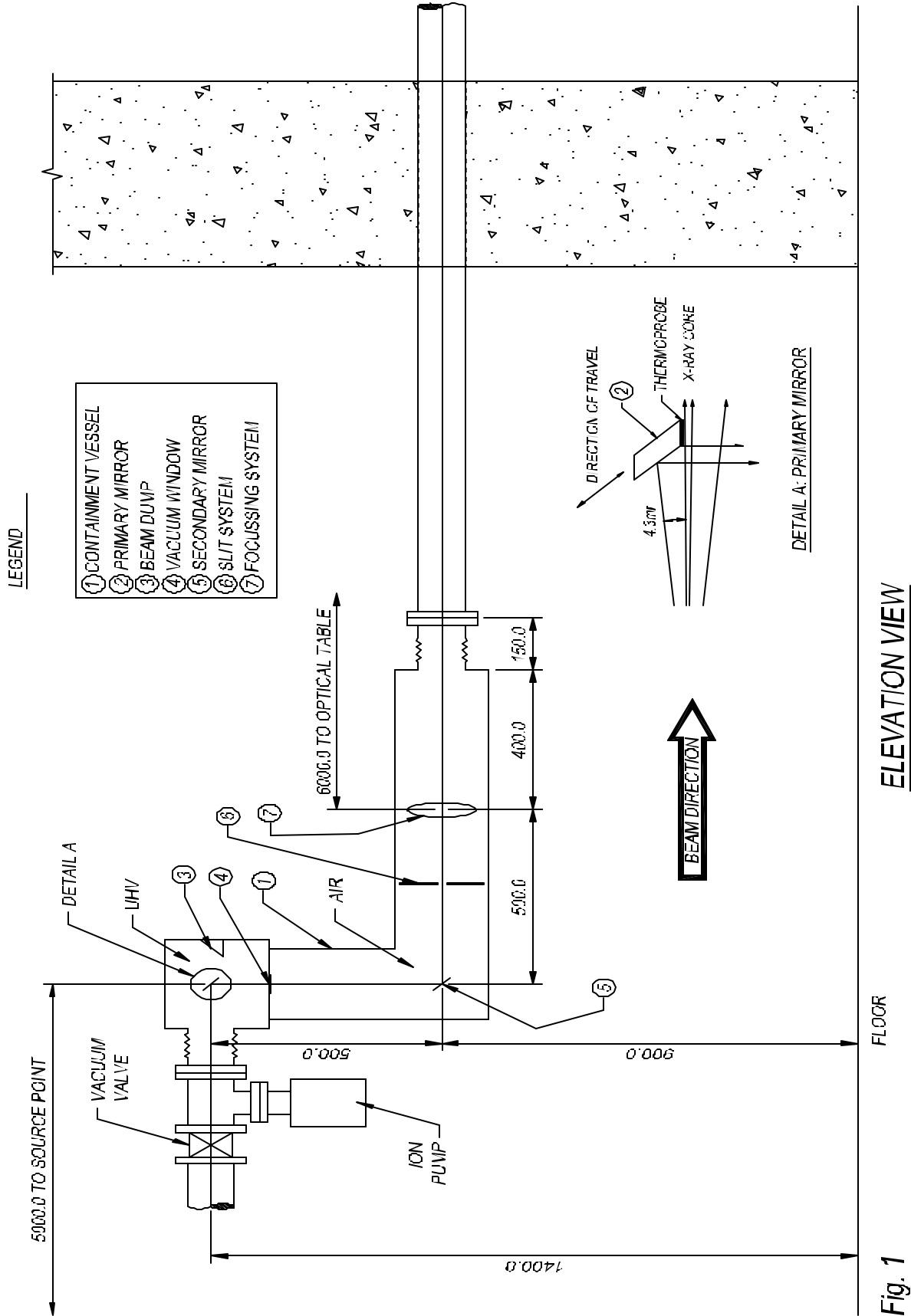
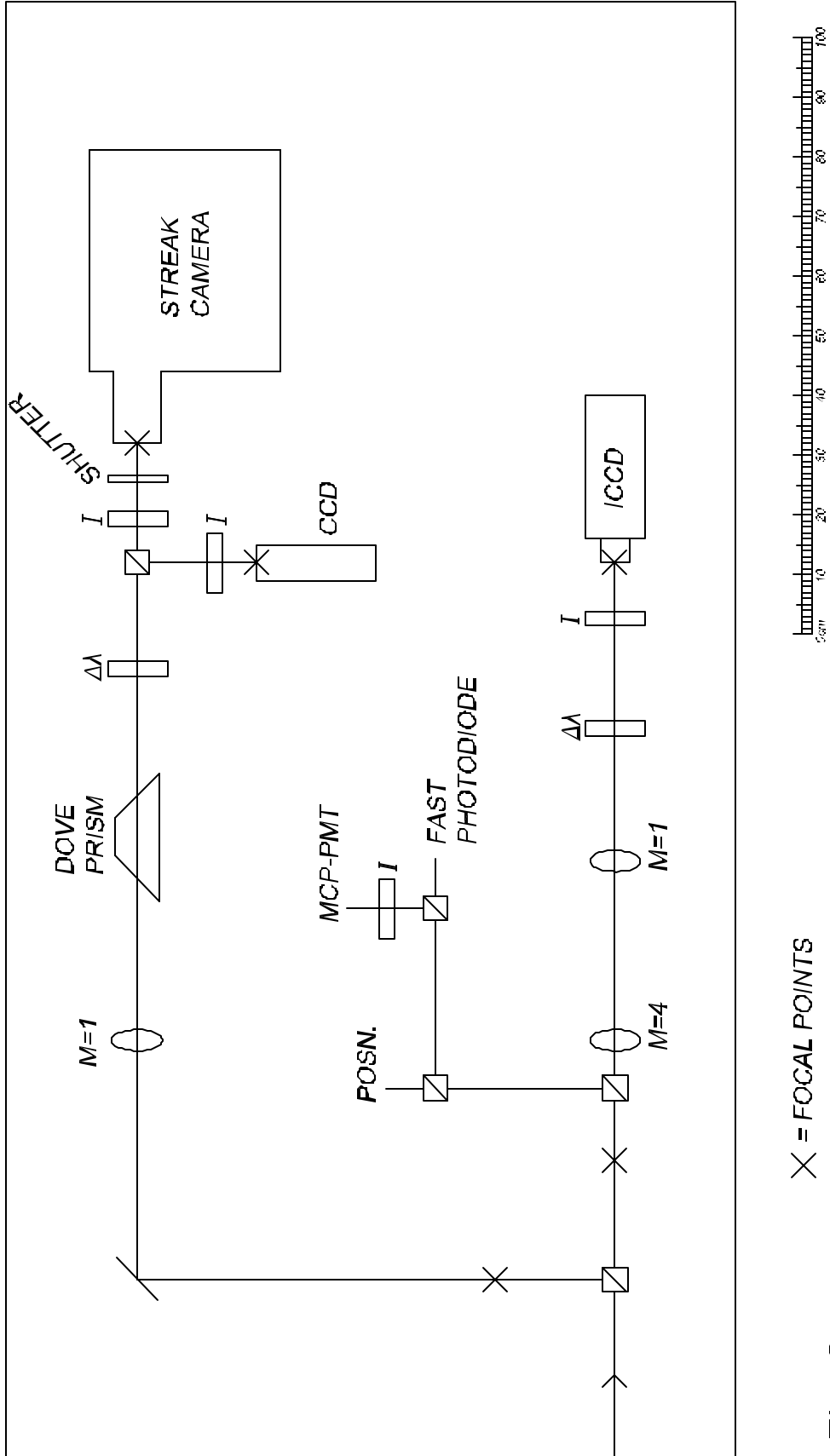


Fig. 1



X = FOCAL POINTS

Fig. 2

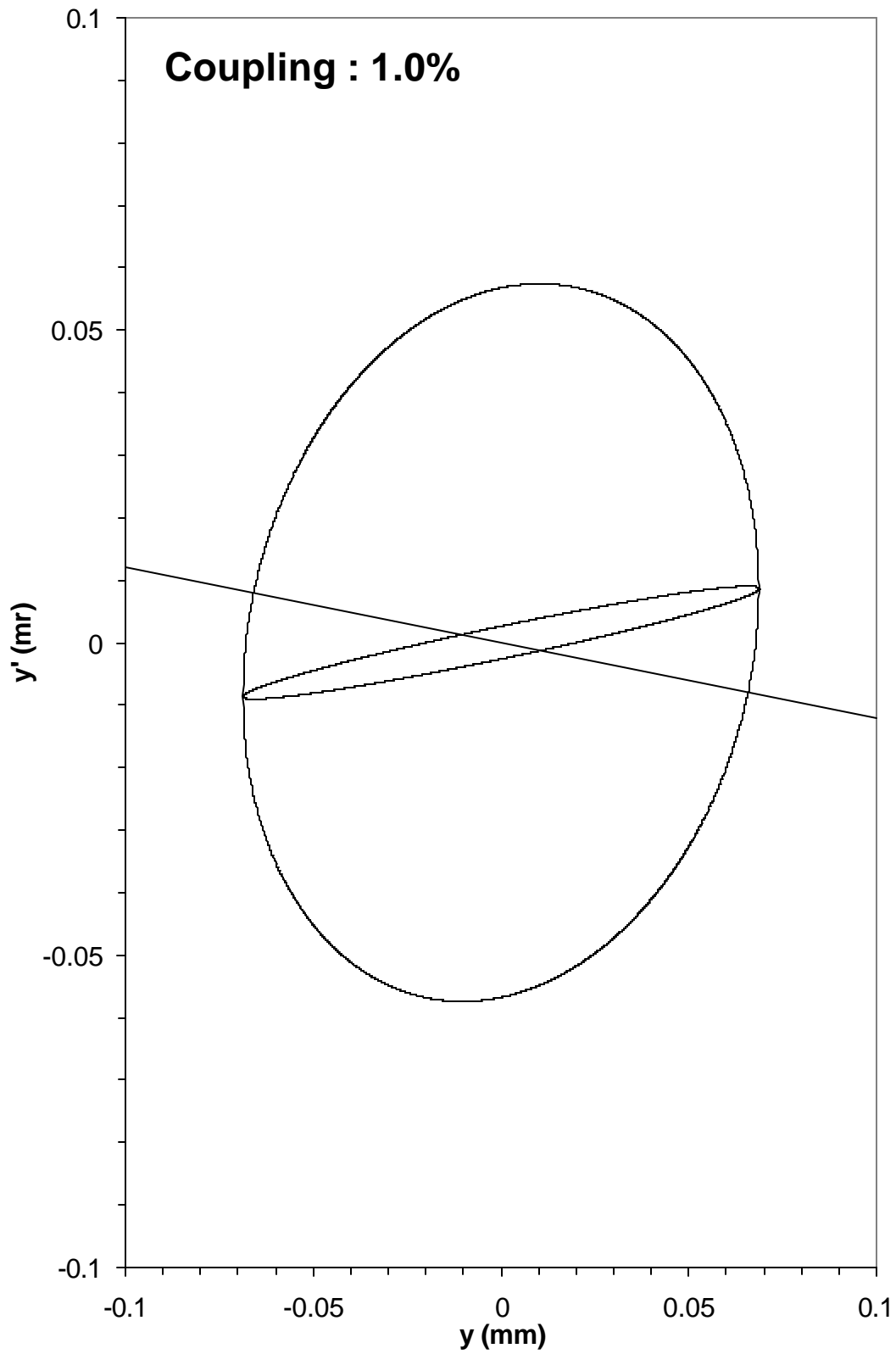
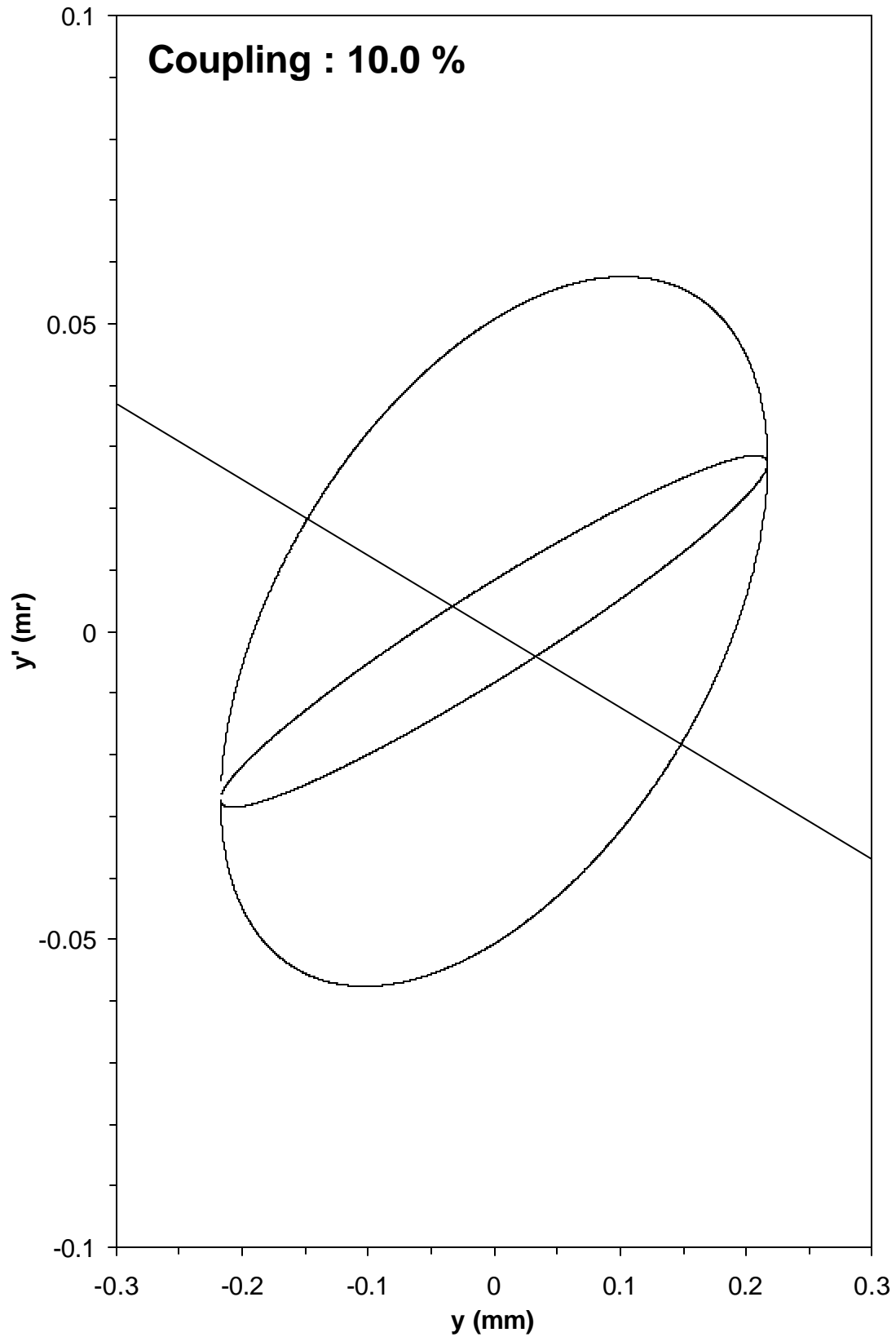


Fig. 3a

**Fig. 3b**